EES Solar

Accepted Manuscript

This article can be cited before page numbers have been issued, to do this please use: F. Liang, F. Abdi and R. van de Krol, *EES Sol.*, 2026, DOI: 10.1039/D6EL00057F.

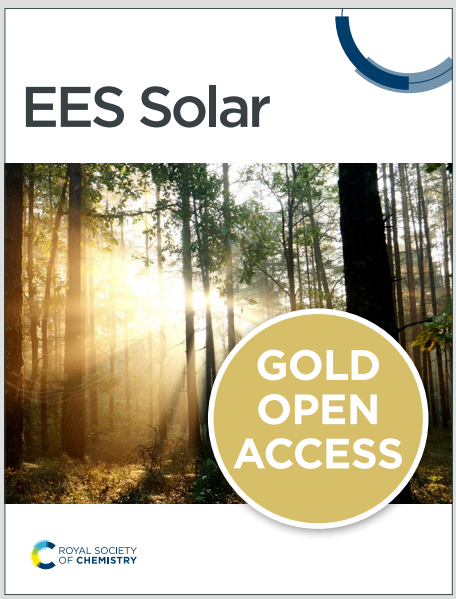

View Article Online
DOI: 10.1039/D6EL00057F

Electrochemical processes powered by renewable power sources, such as sunlight, will become a cornerstone of the future energy infrastructure. Photoelectrochemical devices combine light absorption and electrochemical conversion in a single device or even a single material. While the efficiencies of new absorber materials and co-catalysts for photoelectrochemical processes have markedly improved over the past years, scale-up efforts to active areas larger than a few cm^2 are still hindered by mass transport limitations. Such limitations manifest not only in reduced efficiencies but also in materials degradation due to the formation of pH gradients. Other challenges include electrode deactivation due to bubble formation and product crossover, especially in the case of membrane-less devices. While some of these challenges are similar to those encountered for commercial electrolyser systems, different solution strategies are needed because i) the requirement of illuminating at least one the electrodes requires a different device architecture and ii) PEC devices operate at 50-100x lower current densities. Numerical multiphysics simulations have provided useful insights in these losses but are not (yet) able to capture all relevant physical processes in PEC devices. There is, therefore, an urgent need for analytical tools that provide direct experimental insight into mass transport-related phenomena in PEC devices. This study presents recently developed experimental methods that can help to close this gap.

View Article Online
DOI: 10.1039/D6EL00057F

ARTICLE

In situ measurement of mass transport in (photo)electrochemical water splitting at device scale

Received 00th January 20xx,
Accepted 00th January 20xx

DOI: 10.1039/x0xx00000x

Feng Liang,[a,b,c] Fatwa F. Abdi[a,d*], Roel van de Krol[a,e*]

Understanding the transport of ions and dissolved gasses in aqueous solutions is crucial for the scaling-up of photoelectrochemical (PEC) energy conversion devices. In this study, we performed *in situ* measurements of the pH distribution and the dissolved oxygen concentration during water electrolysis, under realistic conditions for PEC water splitting devices. The influence of forced electrolyte convection on the mass transport processes was analyzed using particle image velocimetry (PIV) to capture the instantaneous electrolyte flow velocity fields. The measurements reveal a ΔpH of ~3 in 0.1 M KP_i buffer solution (pH 7) at 10 mA cm^{-2}, corresponding to a Nernstian overpotential of ~200 mV. While this detrimental loss can be mitigated by recirculating the mixed electrolyte, the use of higher buffer concentrations is found to be an even more effective strategy. At low flow rates, the pH gradient-induced overpotentials are significantly lower than those predicted by previously reported 1D multiphysics simulations. *In situ* observations of dissolved oxygen during water splitting demonstrate that the forced convection enhances oxygen removal and reduces the hazardous risk of product crossover. These quantitative findings can guide the rational design of highly-efficient, scalable PEC water splitting devices.

Introduction

Photoelectrochemical (PEC) water splitting offers a direct pathway to convert intermittent solar energy into chemical fuels, such as hydrogen and hydrocarbons.[1, 2] The scaling up of PEC water splitting devices remains challenging and several approaches have been explored, including increasing the photoactive area per device,[3] parallel operation of multiple devices,[4, 5] and/or using solar concentration.[6, 7] Large-area devices tend to deliver much lower STH efficiencies (by a factor of up to ~5) compared to their small-area equivalents.[8] For instance, it has been reported that the 6% STH efficiency of small-area (0.24 cm^2) $BiVO_4$-based tandem devices decreases to ~2% when scaling up the active area to 50 cm^2.[3] This significant loss of efficiency has been attributed not to any degradation in materials quality of the large-area $BiVO_4$ photoanode but to mass-transport limitations in the electrolyte (proton/hydroxide ions). Ohmic losses in the transparent conducting substrate also play a role but account for only 10-15% of the voltage losses at these relatively modest photocurrent densities. Ion transport-related losses become increasingly important in PEC systems operated at near-neutral pH conditions, which attract interest due to the instability of many semiconducting materials in highly acidic and/or highly alkaline solutions. At around pH 7, the proton/hydroxide ion concentration is low (less than a µmol L^{-1}) and the reactants will be depleted rapidly. Moreover, at such low concentrations resupply of the reactants from the neighbouring bulk electrolyte will not be able to keep up due to diffusion limitations. This results in concentration overpotentials in addition to the kinetic overpotentials from the electrocatalysts.[9] Although supporting buffer ions (e.g., phosphate, bicarbonate, etc.) can locally provide or take up H^+/OH^-, the combination of the concentration and the diffusion coefficients of these ions are typically too small to prevent the formation of pH gradients.[3, 10] Complementary studies further highlight that such mass transport heterogeneities are closely coupled with bubble accumulation and interfacial degradation behaviour, which severely compromise the long-term durability and scalability of practical (P)EC systems.[11-15] Understanding the local pH shift during OER and HER reactions is therefore of crucial importance for the development of efficient solar energy conversion devices in near-neutral pH solutions.

In addition to the ion transport-related losses, another important yet often overlooked aspect is the transport of dissolved species (e.g., H_2 and O_2) during (P)EC water splitting. For example, gas crossover during water electrolysis will lower the purity of the products and may lead to safety concerns (the explosion limit for hydrogen is only 4%). These considerations are especially important for membrane-less PEC cell designs. The removal of dissolved O_2 and/or H_2 product gases via e.g. forced flow would mitigate these concerns and improve the overall efficiency. Being able to measure the local

[a] Institute for Solar Fuels, Helmholtz-Zentrum Berlin für Materialien und Energie GmbH, Hahn-Meitner-Platz 1, 14109 Berlin, Germany.
[b] School of Mechanical Engineering, Xi'an Jiaotong University, No.28 Xianning West Road, Xi'an, Shaanxi 710049, China.
[c] State Key Laboratory of Multiphase Flow in Power Engineering, Xi'an Jiaotong University, Xi'an 710049, China
[d] School of Energy and Environment, City University of Hong Kong, 83 Tat Chee Avenue, Kowloon, Hong Kong SAR, China.
[e] Institut für Chemie, Technische Universität Berlin, Straße des 17. Juni 124, 10623 Berlin, Germany.
† Footnotes relating to the title and/or authors should appear here.
Supplementary Information available: [details of any supplementary information available should be included here]. See DOI: 10.1039/x0xx00000x

concentrations of dissolved O_2 and/or H_2 would help the development of effective gas removal strategies and to get a better understanding of the overall reaction kinetics.

Theoretical models have been devised to simulate mass transport and predict efficiency losses in energy conversion systems. Singh et al. investigated the effect of various flow schemes for near-neutral pH electrolytes in solar-fuel generators, and showed that the convective mixing of anolyte and catholyte can greatly reduce pH gradients and the corresponding concentration polarization losses.[16, 17] Using multiphysics modelling, Obata et al. found that bubble-induced convection can stabilize the pH gradients near gas-evolving electrodes [18] and that product crossover can be suppressed using modest flow rates, even for devices with tilt angles of 30° versus the horizontal plane.[19] Abdi et al. investigated voltage losses in a PEC device with 8 cm long electrodes, and reported that about 25% of the 600 mV overpotential needed to sustain a current density of 10 mA cm^{-2} is due to concentration polarization.[20] Liang et al. explored the effect of device operating pressure on the pH gradient-induced voltage losses, and found that although bubble evolution can be effectively suppressed by increasing the pressure, no significant impact of pressure on the concentration overpotential is observed.[13] It should be noted that these multiphysics simulations typically require a large number of simplifying assumptions to be made (e.g. laminar flow, constant bubble formation efficiency), which means that rigorous validation is needed before they can be used as guidelines for the actual design of PEC cells.

Complementary to modelling and simulation studies, several experimental approaches have been reported to determine local pH shifts using electrochemical methods, such as rotating ring disk electrodes (RRDE) and scanning electrochemical microscope (SECM) measurements,[21-26] or spectroscopic methods, such as surface-enhanced infrared absorption spectroscopy (SEIRAS) and fluorescence spectroscopy.[27-39] Most of those techniques utilize ultramicroelectrodes to directly monitor the pH change in the vicinity of model electrodes, providing detailed insights into interfacial processes at electrode-electrolyte interfaces. Although many of the insights are transferrable, the design of practical P(EC) devices requires understanding of pH gradients and mass transport limitations at macroscopic length scales. Various attempts have been undertaken to visualize pH gradients and mass transport in real systems. Obata et al. conducted *in situ* fluorescence measurements to visualize the pH distribution in a static electrochemical cell with cm-scale electrodes, and identified the key role of buoyancy-driven convection in stabilizing the local pH gradient.[40] Radhakrishnan et al. were able to show natural convective mass transfer of dissolved oxygen during water splitting, for various electrode configurations.[41]

Forced electrolyte flow is widely recognized as an effective strategy to mitigate pH gradient during water electrolysis.[16, 17, 20, 42, 43] However, to the best of our knowledge, only one study has experimentally quantified the impact of forced convection on pH gradients during water splitting, employing in-line Raman spectroscopy to measure the pH at the interface in real-time.[44] These results, however, were obtained at high current densities (200 mA cm^{-2}) for a 0.5 cm^2 sample, whereas practical PEC cells with cm-scale (photo)electrodes operate at current densities of 10 – 20 mA cm^{-2}. Apart from this study, no quantitative PEC reports exist on the effect of forced flow on pH gradient and dissolved species. This gap represents a critical disconnect between the mechanistic understanding of the mass transport phenomena and the rational optimization of state-of-the-art PEC cells and their components.[45, 46]

In this study, we build upon the previously reported fluorescence measurement setup [40] to enable *in situ* monitoring of electrolyte flow effects on pH distribution and dissolved oxygen concentration during water splitting. This setup, integrated into a customized flow cell, is complemented by particle image velocimetry (PIV) measurements to visualize the velocity field of the electrolyte flow. We first demonstrate pH changes in both acidic and neutral pH electrolyte solutions, observing a ΔpH exceeding 3 units in both cases, even with electrolyte recirculation at a flow rate of ~3.2 mL cm^{-2} s^{-1}. To mitigate this, increased buffer concentrations are explored as an effective approach to suppress pH shifts. Finally, we present *in situ* measurements of the dissolved oxygen concentration during water electrolysis, providing insights into reaction kinetics and the effectiveness of strategies to mitigate gas crossover risks. These findings offer valuable guidance for the rational design of efficient, scalable solar fuel production devices.

Results and discussions

pH gradient in acidic and neutral pH electrolytes during water splitting

A schematic illustration of the fluorescence measurement setup is shown in Fig. 1a. The water splitting cell is configured with two vertically oriented platinum/FTO electrodes facing each other, with the fluorescence foil sensor (width of ~8 mm) immersed in between and perpendicular to the two electrodes. The *in situ* pH measurements are conducted during galvanostatic operation of the cell at a fixed current density of 10 mA cm^{-2}, representing typical operating conditions for practical PEC water-splitting devices.[47, 48] Note that we deliberately conducted these experiments on dark electrodes, since photoelectrodes that can generate photocurrents of 10 mA cm^{-2} and are stable for many hours are not easily available. Moreover, (simulated) solar illumination would interfere with the homogeneous blue illumination that is required for the fluorescent foil sensors to work. Details about the setup and the measurement parameters are documented in the Experimental section. In brief, the electrolyte is recirculated using a rotary pump and the electrolyte is mixed by flowing through a homogenizer before re-entering the electrochemical cell. A technical drawing and schematic illustration of the setup are shown in Fig. S1, and digital photographs of the setup can be seen in Fig. S2. The electrolyte flow rate is determined by controlling the pumping power of the rotary pump. Unless otherwise specified, the measurements were conducted under atmospheric pressure. Two types of pH foil sensor were used,

View Article Online
DOI: 10.1039/D5EL00057F

one with a pH detection range from 5 to 8, and another from 2 to 5. The calibration curves of the foil sensors are shown in Fig. S3. The working principle of the fluorescence foil sensors is explained in the Experimental section.

The spatially-resolved evolution of the pH during water electrolysis in 0.5 M K_2SO_4 (pH 7) solution is shown in Fig. 1b, at a current density of 10 mA cm^{-2} and an electrolyte flow rate of 3.2 mL cm^{-2} s^{-1}, see also *Supplementary video S1.* Note that we deliberately normalize the volumetric flow rate by the surface cross section between the two electrodes; the indicated rate thus corresponds to a linear flow velocity of 3.2 cm s^{-1}. Fig. 1b clearly shows that the local pH shifts to more acidic and alkaline values at the anode and cathode, respectively, as expected from the half-reactions for water splitting under pH-neutral conditions:

$$\text{Cathode: } 4H_2O + 4e^- \rightarrow 2H_2 + 4OH^- \quad (1)$$

$$\text{Anode: } 2H_2O \rightarrow O_2 + 4H^+ + 4e^- \quad (2)$$

Fig. 1b shows that a significant pH gradient (larger than 3 units) develops within 10 minutes; such large changes are not unexpected for an unbuffered electrolyte (0.5 M K_2SO_4) at pH 7. Note that the local pH close to the electrode surface exceeds the specified detection range of the sensor foil (pH 5 – 8), so the accuracy is reduced in these regions.

The effect of forced convection of electrolyte flow is clearly visible in Fig. 1b; the bulk electrolyte remains pH neutral due to the constant supply of mixed electrolyte from the inlet at the bottom of the cell. Along the height of the electrodes, the effect of electrolyte flow becomes less pronounced due to the hydrodynamic pressure drop. The electrolyte flow velocity field is examined in more detail using particle image velocimetry measurements, see *Experimental* and Fig. S4 for technical details. The results, shown in Fig. S5a, show that the electrolyte velocity gradually decreases along the electrode height. This is indeed consistent with the trend in the pH gradient distribution shown in Fig. 1b.

We then changed the pH of the electrolyte to 3.5 by adding H_2SO_4, while keeping all other parameters the same as for Fig. 1b. We speculate that with a significantly higher proton concentration (~3 orders of magnitude higher compared to pH 7) and the same current density of 10 mA/cm^2, the local changes in pH will be much less pronounced. However, as shown in Fig. 1c, after 10 min the pH changes by about +1.2 units near the cathode surface, similar to the change of about +1.5 units observed for the pH 7 solution. In contrast, the pH changes about 0.3 units close to the anode, compared to the more than 2 units shift observed for the pH 7 solution. The much smaller pH shift at the anode side is due to the fact that 0.5 M H_2SO_4 was used to adjust the electrolyte to be the desired pH (3.5). H_2SO_4 fully dissociates (pK_{a1} = -2) and the resulting HSO_4^- ions act as a buffer. The buffering reactions near the cathode and the anode can be expressed as follows, respectively:

$$HSO_4^- \rightarrow SO_4^{2-} + H^+;\ pK_{a2} = 1.99 \quad (3)$$

$$SO_4^{2-} + H_2O \rightarrow HSO_4^- + OH^-;\ pK_{b2} = 12.01 \quad (4)$$

The starting pH of the solution (pH 3.5) is much closer to the pK_{a2} than to the pK_{b2}, which means that the buffer capacity for H^+ is much larger than for OH^-. This explains why the pH shifts near the anode are much smaller than those near the cathode in Fig. 1c.

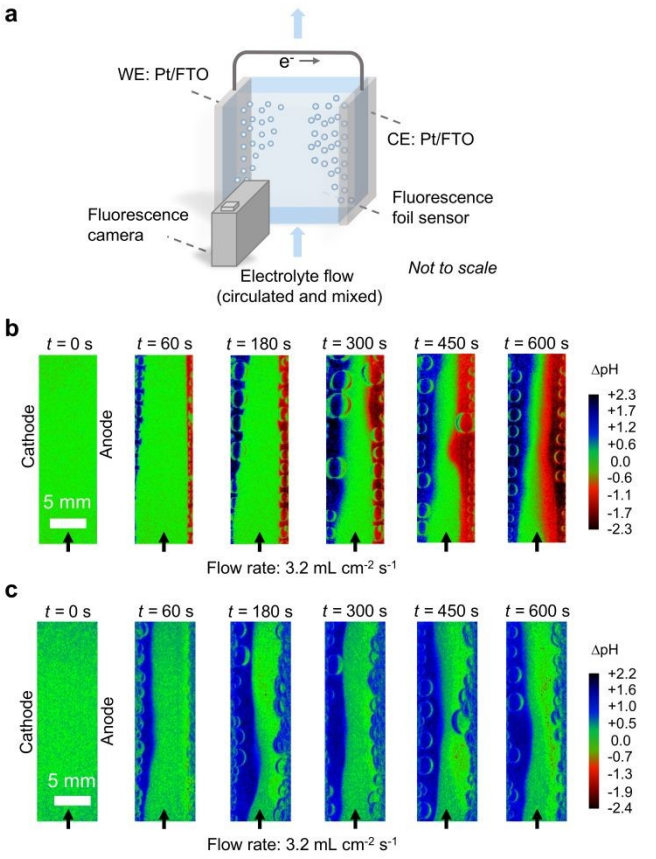

Fig. 1. Schematics of the *in situ* pH measurement setup and the distribution of local pH change (ΔpH) during water electrolysis at 10 mA cm^{-2} and a bottom-to-top flow rate of ~3.2 mL cm^{-2} s^{-1}. (a) Schematic illustration of the measurement setup, (b) ΔpH evolution in 0.5 M K_2SO_4 with an initial pH of 7, (c) ΔpH evolution in 0.5 M K_2SO_4 with an initial pH of 3.5 (electrolyte pH of ~6.8 as prepared, titrated to pH 3.5 by adding 0.5 M H_2SO_4). The water splitting cell is configured with two parallel-facing platinum/FTO electrodes, with a gap of 8 mm. Two different types of pH foil sensor are used, one with a pH detection range from 5 to 8 (used for panel b), and another from 2 to 5 (for panel c). The experiments are conducted at atmospheric pressure (0 barg).

With a pH shift well over 2 pH units—and possibly more, in view of the limited pH range of the sensor foil—the Nernstian overpotential is significant (> 120 mV) and will adversely affect the overall efficiency of the PEC device. Several possibilities exist to mitigate this loss mechanism. One option is to apply a higher electrolyte flow rate.[16, 42, 49] The flow rate used in Figs. 1b and 1c is 3.2 mL cm^{-2} s^{-1}, which translates into an average linear fluid velocity of ~3.2 cm s^{-1} in the electrode region. Numerical calculations by Abdi et al. showed that an inlet velocity of 4 cm s^{-1} is sufficient to limit the concentration overpotential to less than 20 mV, although these calculations assumed a higher buffer concentration (2 M KP_i).[20] A second option is to use stronger acid or alkaline electrolyte solutions. For PEC water electrolyzers, however, this option is of limited use due to the instability of many semiconducting materials in strong acidic or alkaline solutions. A more realistic option is to use a pH buffer with stronger buffer capacity.[50] Phosphate and borate buffers,

View Article Online
DOI: 10.1039/D5EL00057B

for example, have been shown to effectively minimize pH shifts during water splitting, even for relatively low buffer concentrations of 0.1 M.[40]

Effect of flow rate on pH gradient

We now change the electrolyte to 0.1 M KP_i (pH 7) and investigate the effect of flow rate on pH gradient, again at a current density of 10 mA cm^{-2}. The evolution of the pH colormaps during the *in situ* measurements at electrolyte flow rates of 0, 1.5, and 3.2 mL cm^{-2} s^{-1} are shown in Fig. 2a-c. The corresponding pH profiles between anode and cathode, recorded at different times, are shown in Fig. 2d-f. As shown in Fig. 2a, even at zero flow, the use of a 0.1 M KP_i buffer significantly reduces the pH gradient compared to that in 0.5 M K_2SO_4 at ~3.2 mL cm^{-2} s^{-1} (see Fig. 1b). This confirms our previous findings[40] and illustrates the effectiveness of using suitable pH buffers, even at relatively high current densities (the 10 mA cm^{-2} current density used here is about 10× higher than in Ref. [40]). Figures 2a-c also indicate that the pH gradient decreases as the flow rate increases. This is further quantified in Fig. 2d-f, which shows that the total pH gradient between the cathode and anode reduces from 2.5 pH units under static conditions (zero flow) to about 1.5 units at a flow rate of 3.2 mL cm^{-2} s^{-1}. A higher flow rate also means that steady state conditions are reached faster; about 180 s in the absence of flow (Figs. 2a, d) compared to 60 s at a flow rate of 3.2 mL cm^{-2} s^{-1} (Figs. 2c, f). Note that a total pH gradient of 1.5 pH units implies polarization losses of about 100 mV, which is still considerable. In other words, even a combination of mixing, recirculation, and the use of a pH buffer with low concentration (e.g., 0.1 M KP_i) is not sufficient to fully suppress polarization losses in PEC water splitting cells with an electrode spacing of 8 mm and operating at 10 mA cm^{-2}.

As shown in Figs. 2a-c, the average width of the ΔpH layer decreases with increasing flow rate, consistent with a more rapid removal of (de)protonated species by the bulk flow. Figs. 2a-c also reveal that there are strong local variations in the pH gradient due to bubble evolution at the electrode surface. As previously reported, the local stirring effect induced by ascending bubbles strongly disturbs the near-electrode distribution of H^+ and OH^- ions.[18] These local variations also explain the unexpectedly large thickness of the ΔpH layer width in Fig. 2e, which was determined from three lines-of-interest along the electrode height and is therefore relatively sensitive to local variations.

The ΔpH profiles in 1 M KP_i buffer are shown in Fig. 3 for three different electrolyte recirculation rates: 0 mL cm^{-2} s^{-1}, 1.5 mL cm^{-2} s^{-1}, and 3.2 mL cm^{-2} s^{-1}. The colormaps are shown in Fig. S6 and a movie of the process can be seen in *Supplementary video S2-S4*. With the higher KP_i buffer concentration, the pH gradient is indeed suppressed. For example, without recirculation of the electrolyte, the total ΔpH decreases from 2.5 for the 0.1 M KP_i buffer solution (Fig. 2d) to less than 1 for the 1 M KP_i buffer solution (Fig. 3a). The ΔpH can be reduced further by increasing the flow rate and becomes negligible at a flow rate of 3.2 mL cm^{-2} s^{-1} (see Fig. 3c and the colormaps in Fig. S6c). These findings clearly show that the formation of pH gradients can be almost completely suppressed by combining a sufficiently high buffer concentration with a high enough flow rate. However, it should be noted that changing the buffer concentration will also affect the gas bubble dynamics during (P)EC water electrolysis. Specifically, the average bubble diameter decreases with increasing buffer concentration, as reported by Qiu et al.[51] For PEC water splitting devices, especially in cell configurations in which the light needs to pass through the electrolyte to reach the photoelectrodes, a higher density of small gas bubbles is generally problematic as they tend to attenuate the light more than larger bubbles.[13, 52] Therefore, more quantitative investigations are required to assess the tradeoffs associated with choosing the optimal buffer concentration.

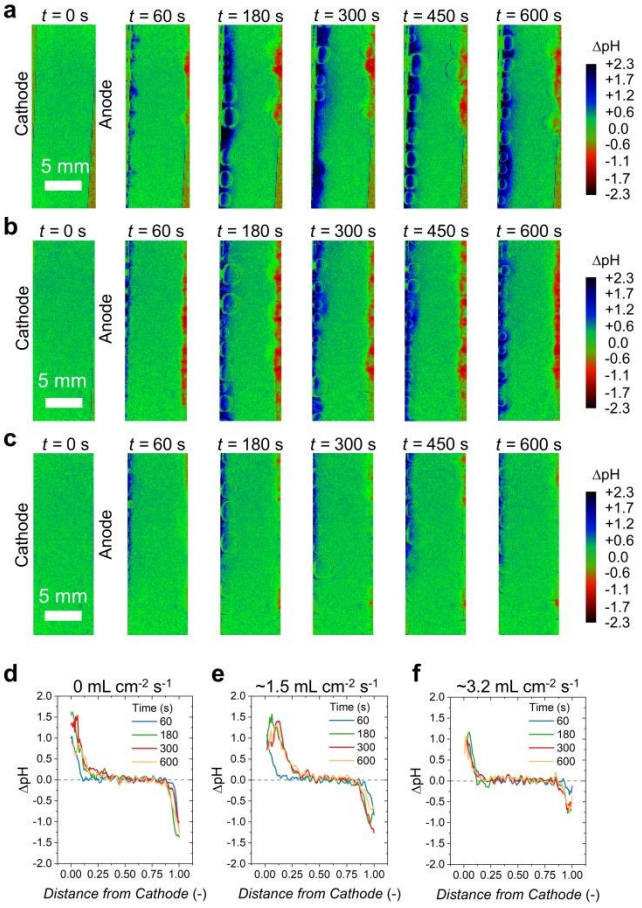

Fig. 2. The change in the pH distributions (ΔpH) and pH profiles during water electrolysis in 0.1 M KP_i buffer solution at 10 mA cm^{-2}. Colormaps of ΔpH of the electrolyte (a) in absence of electrolyte flow, (b) 1.5 mL cm^{-2} s^{-1} electrolyte flow rate, (c) 3.2 mL cm^{-2} s^{-1} electrolyte flow rate. (d)-(f) show the pH profiles at electrolyte flow rate of 0, 1.5, and 3.2 mL cm^{-2} s^{-1}, respectively. The pH profiles are measured along the horizontal distance between the two electrodes, and averaged among at least three *lines-of-interest* along the electrode height. The initial pH of the electrolyte is 7. Note that the distance between the cathode and anode is 8 mm, with panels d-f showing the normalized values.

View Article Online
DOI: 10.1039/D5EL00057F

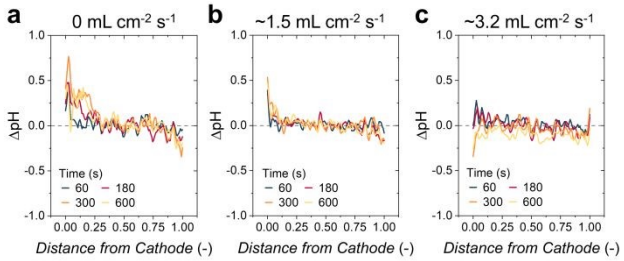

Fig. 3. Evolution of ΔpH during water electrolysis in 1 M KP_i buffer solution. ΔpH profiles (a) in absence of electrolyte flow, and at electrolyte flow rates of (b) 1.5 mL cm^{-2} s^{-1} and (c) 3.2 mL cm^{-2} s^{-1}. The initial pH of the electrolyte is 7. The current density is kept constant at 10 mA cm^{-2}.

Effect of elevated pressure on pH gradient

We recently evaluated the influence of operating pressure on the efficiency of PEC devices.[13, 47, 48] While operation at elevated pressure can benefit the overall efficiency, the simulations showed that pressure does not have a significant effect on the pH gradient-induced overpotential. Specifically, for an electrolyte flow rate of 12 mL cm^{-2} s^{-1} and assuming fully developed laminar flow, the simulated concentration overpotential increased by about 1 mV when increasing the pressure from 1 bar to 10 bar.[13] To experimentally verify these simulations, the pH gradient was measured *in situ* during water electrolysis at ambient pressure (0 barg) and at elevated pressure (4 barg). The ΔpH profiles after 10 minutes of measurement are shown in Fig. 4 for various flow rates, while the colormaps are shown in Fig. S7. Although there is some scatter in the data, the ΔpH profiles do not show large differences at 0 barg vs. 4 barg. This confirms that increasing the operation pressure of PEC devices has a negligible influence on the concentration overpotential. As discussed earlier, the use of electrolyte flow has a much larger influence; the ΔpH between anode and cathode decreases from ~2 under zero flow (Fig. 4a) to about 1 at 3.2 mL cm^{-2} s^{-1} (Fig. 4c). This corresponds to a flow-induced reduction in the Nernstian overpotential of about 60 mV, independent of the operating pressure.

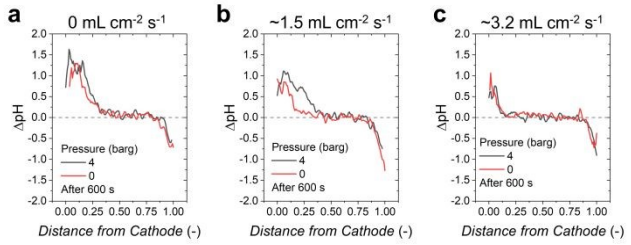

Fig. 4. ΔpH profiles after 600 s of water electrolysis at operating pressures of 0 barg (red) and at 4 barg (black). ΔpH profiles (a) in absence of electrolyte flow, (b) 1.5 mL cm^{-2} s^{-1} flow rate, (c) 3.2 mL cm^{-2} s^{-1} flow rate. A 0.1 M KP_i buffer solution (initial pH of ~7) is used as the electrolyte in both cases, and the cell is operated in galvanostatic mode with a current density of 10 mA cm^{-2}.

pH recovery measurement

Forced electrolyte convection also affects the recovery of the pH when the (P)EC process is stopped. We investigated this by conducting the following experiment. First, water electrolysis is conducted at 10 mA cm^{-2} in 0.1 M KP_i buffer (pH = 7) for 10 minutes, at a flow rate of 1.5 mL cm^{-2} s^{-1}. Then, the current is switched off while the electrolyte is kept circulating for about 1 hour, see the *J-t* curve in Fig. 5a. The pH gradient is monitored *in situ* during the entire process. The purpose of this experiment is to check how fast the pH gradient disappears due to recirculation and mixing. The flow rate of 1.5 mL cm^{-2} s^{-1} is selected because previous simulation work has demonstrated that the near-electrode pH gradient becomes negligible under these flow conditions.[16] To minimize the influence of gas bubbles, this experiment is conducted at an overpressure of 4 barg (= 5 bar absolute pressure). Under these conditions, the pH gradient is mainly determined by the interplay between buoyancy-driven convection[40] and forced convection. Colormaps of the pH gradient at different times are shown in Fig. 5b, with the average pH at the electrode surfaces shown in Fig. 5a. The recorded movie can be found in *Supplementary video S5*. The corresponding electrolyte flow velocity field is shown in Fig. S8.

Clearly, as shown in Fig. 5b, a significant pH gradient (ΔpH ≈ 2) develops after 10 minutes at 10 mA cm^{-2}. A closer look at the pH colormaps reveals more distinct features in the pH gradients near the cathode and the anode. The pH gradient near the cathode widens at about half the height of the cell and becomes narrower at the upper half. In contrast, at the anode side a mass transport boundary layer appears that continuously thickens towards the outlet of the channel (see Fig. 5c). This difference can be explained as follows. During electrolysis, the local pH at the cathode becomes more alkaline. In a phosphate buffer solution, this is compensated by an increase in the concentrations of dibasic (K_2HPO_4) and tribasic (K_3PO_4) phosphate. Since K_2HPO_4 and K_3PO_4 have a higher mass density than the 0.1 M KP_i buffer solution in the bulk,[40, 53, 54] the electrolyte near the cathode's surface initially flows downward. When approaching the inlet, the flow is directed upward again under the influence of forced convection in the bulk, see Fig. 5b,c and *Supplementary video S5*. The opposite is true for the electrolyte near the anode, i.e., the electrolyte near the anode becomes less dense. The forced electrolyte flow (visible in Fig. S8) thus confines the electrolyte to the vicinity of the anode, thereby forming boundary layer that impedes mass transfer.

By continuously recirculating the mixed electrolyte after terminating the water electrolysis reactions, the pH gradient gradually reduces. As shown in Fig. 5a, b and *Supplementary video S5*, it takes about 12 minutes for the pH gradient to (almost) completely disappear in the region near the cathode after stopping the electrolysis reactions. Recovery at the anode is slower, with the gradient remaining present even after more than one hour. Such a slow pH re-equilibration process is somewhat unexpected, as the electrolyte is recirculated and well mixed. The reason for the slow recovery at the anode is the presence of the boundary layer, where the large velocity difference between the bulk electrolyte and the near-stagnant region impedes mass transfer. The much faster recovery at the cathode is primarily due to the low electrolyte velocity (Fig. S8) in the region where the upward and downward flows mix (white arrows in Fig. 5b). A lower velocity difference between two distinct flow regions enables faster mass transfer across the

View Article Online
DOI: 10.1039/D5EL00057E

boundary between the regions. The mass transfer is thus primarily limited by the presence of these boundary layers and less by the bulk flow rate.

We briefly note that we also checked the response time of the foil sensor itself. As shown in Fig. S9, it takes less than a minute for the foil sensor to indicate local pH changes, both for the anode and the cathode side. This is consistent with the response time according the foil sensor specification (<30 seconds). Thus, the temporal evolution of the pH shown in Fig. 6 is not limited by the response time of the sensor foil.

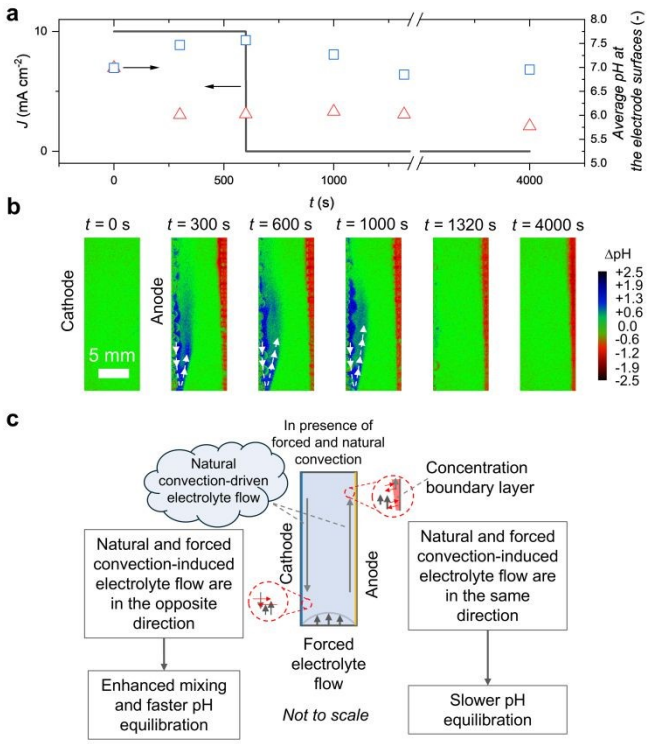

Fig. 5. pH gradient recovery measurement. (a) *J-t* curve during the pH recovery measurement and the average pH at the electrode surfaces. (b) Time-sequenced ΔpH colormaps. (c) Schematic illustrations of the different pH equilibration processes at the cathode and anode. The white arrows in (a) indicate electrolyte flow at the vicinity of the cathode. Note that the electrolyte flow near the cathode initially proceeds downward and is subsequently directed upward under the influence of forced convection in the bulk. The cell is operated at a constant current density of 10 mA cm^{-2} for the first 10 minutes, after which the current is switched off. The electrolyte flow rate is fixed at 1.5 mL cm^{-2} s^{-1} for the entire duration of the experiment. The electrolyte is 0.1 M KP_i (pH 7) and the experiment is conducted at room temperature, at a pressure of 4 barg.

Implications for device design: what matters most?

To better understand which factors have the largest influence on the pH gradient, we have consolidated the data by plotting the maximum pH differences that occur in the cell as a function of various operational conditions. The results are shown in Fig. 6a-d. The first parameter of interest is the pH of the solution. As shown in Fig. 6a, an excessive pH gradient (exceeding 3 pH units) can form in a neutral, unbuffered electrolytes, even when the electrolyte is recirculated at a flow rate of 3.2 mL cm^{-2} s^{-1}. Fig. 6a also shows that this pH gradient can be effectively suppressed by titrating the solution to a lower pH. An even more effective approach to reduce concentration overpotentials is to use pH buffers (Fig. 6b). However, this often-employed strategy becomes ineffective when the buffer concentration is too dilute; the example of Fig. 6b shows that reducing the buffer concentration from 1 M to 0.1 M KP_i increases the ΔpH from less than 0.5 units to about 1.5 units. The third parameter that can be varied is the pressure at which the device is operated. Fig. 6c shows that operation at elevated pressure exerts a minimal impact on the pH gradient, consistent with the discussion above and with our previous report.[13] The final parameter is the flow rate, shown in Fig. 6d. As expected, the pH gradient reduces with increasing flow rate. However, with a ΔpH decrease of only 20% when increasing the flow rate from 0 to 3.2 mL cm^{-2} s^{-1}, the effect is relatively small. Clearly, the most effective way to minimize pH gradients and concentration overpotential losses in PEC devices is to operate them at either low or high pH, or to use pH buffer with a sufficiently high concentration (>0.5 M).

The relatively modest change in ΔpH when increasing the flow rate seems surprising when comparing our data to the numerical simulation studies of Singh and co-authors.[16] They reported a sharp decrease in the ΔpH above certain minimal flow rates, as illustrated in Fig. 6e. Their calculations were done using a 1D multiphysics model, assuming similar conditions as our experimental data in Fig. 6f (10 mA cm^{-2}, pH ~7, 1 M phosphate buffer, recirculated and well mixed electrolyte). At flow rates below 0.02 mL cm^{-2} s^{-1}, their calculated ΔpH value rapidly increases to several units, whereas our measured ΔpH at zero flow remains below 0.5 units. One important difference in both methods is that numerical simulations report the pH values directly adjacent to the electrode,[44, 55] whereas the experimentally determined pH values represent the environment at larger distances from the electrode surface (typical a few tens to hundreds of micrometers, due to the limited optical resolution of the camera and limited precision in the placement of the pH sensor foil). To verify which approach best describes the actual electrochemical behavior, we compare chronopotentiometry data recorded at two different flow rates (Fig. 6g). The potential difference is less than 30 mV (which corresponds to a ΔpH smaller than 0.5), which suggests that the experimentally measured pH gradients are the more relevant ones. A possible explanation for the overestimation of the ΔpH by the numerical simulations is the use of a 'fixed wall' boundary condition. This implies zero electrolyte velocity at the solid-liquid interface and tends to overestimate near-electrode pH heterogeneities under low-flow conditions.

These findings highlight the need of combining both experimental data and numerical simulations. Numerical simulations can be easily implemented to obtain a good first-order estimation of the concentration overpotentials. However, the rapid increase of the pH gradient at flow rates lower than ~0.05 mL cm^{-2} s^{-1} seems inconsistent with the measured electrode potentials and suggests that pH gradient simulations at such extremely low flow rates should be treated with caution. Measuring pH gradients with fluorescent pH foil is arguably more cumbersome and lacks the spatial resolution of numerical methods but the data are consistent with the measured overpotentials even at very low flow rates. Moreover, experiments can capture pH gradients under conditions that are

View Article Online DOI: 10.1039/D5EL00057F

still difficult to capture in numerical simulations (such as non-fully developed laminar flow or turbulent flow conditions).

Finally, we note that the fluid dynamics in our experimental cell might be affected by the presence of the foil sensor. We therefore checked the electrolyte flow velocity field with and without inserting the foil sensor using PIV measurements and three-dimensional fluid dynamics simulations. The results are shown in Fig. S5. While the inserted physical foil does disturb the local flow velocity, its influence on the overall flow field is minor, as evidenced by the mid-plane velocity colormaps. Specifically, the average mid-plane flow velocity slightly decreases from 4.76 cm s^{-1} to 4.7 cm s^{-1} after inserting the foil sensor, see Fig. S5e-f. Therefore, the disturbance of the foil sensor to the electrolyte flow can be safely ignored in our measurements.

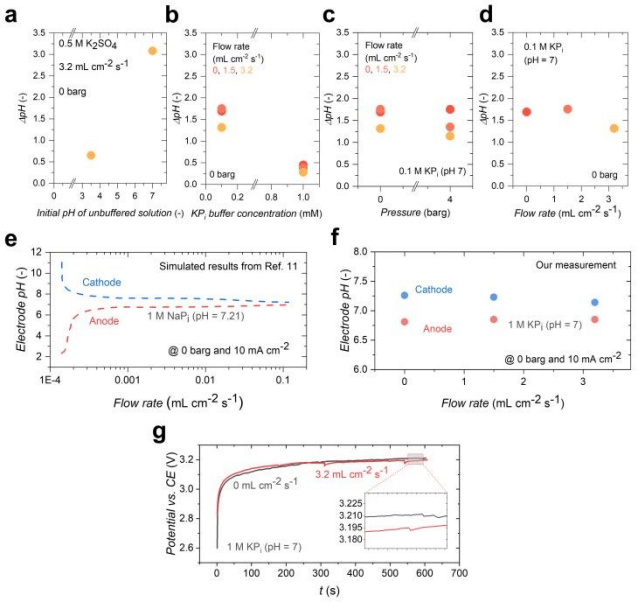

Fig. 6. Electrode pH and the ΔpH as functions of different operational conditions. (a)-(d) show the ΔpH as functions of the initial pH of the unbuffered solution, flow rate, KP_i concentration, pressure, respectively. (e) Simulated electrode pH at anode and cathode as a function of flow rate (data from 1-dimensonal multiphysics simulation reported in ref.[16]) compared with (f) the measured electrode pH in our experiments. (g) Chronopotentiometry curves at 0 and 3.2 mL cm^{-2} s^{-1}, respectively. Note that the current density is kept at 10 mA cm^{-2} for all cases. A 1 M NaP_i buffer solution (initial pH = 7.21) is used as the electrolyte in the simulation of ref. [16], while 0.1 or 1 M KP_i (initial pH = 7) solutions are used for our experiments.

in situ observation of the dissolved oxygen during water electrolysis

Understanding the effect of forced convection of the electrolyte solution on the transport of the dissolved product species during electrolysis is essential to better understand the reaction kinetics and to identify the risk of the hazardous gas product crossover in (P)EC water splitting devices, especially when a membrane-free design is considered. We used our fluorescence measurement setup to investigate the lateral transport of the dissolved oxygen between the two electrodes for static conditions and using forced electrolyte flow. The calibration results of the oxygen foil sensor are shown in Fig. S3c. The dissolved O_2 concentration profiles are shown in Fig. 7, and the colormaps can be found in Fig. S10 (see also *Supplementary videos S6-S7*). Fig. 7a presents the results at zero flow rate. After about 5 minutes, the dissolved oxygen has already reached the middle of the channel and starts to become a potential safety hazard. When introducing a flow rate of 3.2 mL cm^{-2} s^{-1}, the presence of dissolved oxygen gas is almost fully confined to the anode side of the cell (Fig. 7b). The suppression of the dissolved O_2 crossover is more clearly visible in Fig. 7c, where the oxygen concentration at the middle of the flow channel ($x = 0.5 \times L_x$) is found to be greatly reduced at a flow rate of 3.2 mL cm^{-2} s^{-1}. This confirms that gas separation can be improved through hydrodynamic control, as reported in several numerical studies.[16, 19, 42] In addition to preventing crossover, the data in Fig. 7a,b also show that the use of forced flow reduces the dissolved oxygen concentration near the anode by a factor of 4, from about 1600 µM to slightly over 400 µM. This favors the gas evolution reaction by shifting the equilibrium of reaction (2) to the right, thereby reducing the thermodynamic potential for the oxygen evolution half-reaction. While the change in potential is modest (about 9 mV for a 4× lower dissolved oxygen concentration according to the Nernst equation), operating (P)EC water splitting devices using a flow cell thus offers a thermodynamic advantage. To judge whether flow-enhanced designs are viable in practice, these benefits need to be carefully balanced against the increase in parasitic power consumption for pumping. A full techno-economic assessment of the net system efficiency is, however, beyond the scope of this work.

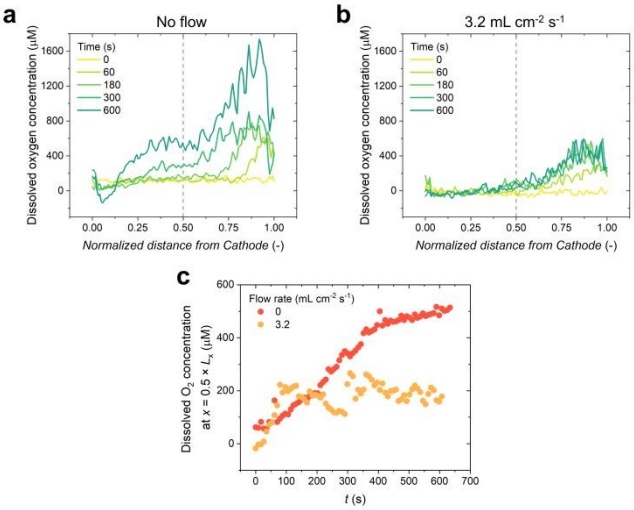

Fig. 7. Profiles of the dissolved oxygen concentration during water electrolysis, obtained from 2D fluorescence imaging data. Dissolved oxygen concentration profiles in the electrolyte (a) in absence of electrolyte flow and (b) at 3.2 mL cm^{-2} s^{-1} electrolyte flow rate. (c) shows the dissolved oxygen concentration at $x = 0.5 \times L_x$ as function of time under different flow rates. The data represent the average of at least three lines-of-interest along the height of the electrode. The dashed lines indicate the midline of the flow channel. The electrolyte is 0.5 M K_2SO_4 (pH = 7), and the electrochemical water splitting cell is operated in galvanostatic mode with a current density of 10 mA cm^{-2}. The distance between the electrodes is 8 mm. The experiment is conducted at room temperature and at atmospheric pressure. Prior to the experiment, the electrolyte was purged by overnight N_2 bubbling to remove any dissolved oxygen. Note that the concentration values are consistent with the reported solubility of O_2 in pure water at 25 °C and atmospheric pressure (1.18-1.25 mM).[56, 57]

We note that the crossover of dissolved *hydrogen* can also lead to efficiency losses and potential safety risks. While the solubility of dissolved hydrogen is less than that of oxygen (0.8 vs. 1.38 mmol L^{-1} at 293 K[58]), its diffusion coefficient in water is more than twice as large as that of oxygen (5.0×10^{-5} cm^2 s^{-1} vs. 2.4×10^{-5} cm^2 s^{-1} at 293 K[59]). Assuming a perfect sink of H_2 and O_2 and the anode and cathode, respectively, filling these numbers into Fick's first law of diffusion yield a 30% higher molar crossover flux for dissolved hydrogen than for dissolved oxygen. While this is within the same order of magnitude, it is clear that hydrogen crossover should be taken into consideration. Unfortunately, fluorescent hydrogen-sensitive foil sensors are not commercially available. Moreover, determining the concentration of dissolved hydrogen in water is actually rather challenging[60] and beyond our current capabilities.

Once the local concentrations of hydrogen or oxygen exceed their respective solubility limits, gas bubbles are formed. The formation and detachment of bubbles induces convection that can benefit mass transport but can also block active sites and scatter light, decreasing the overall device efficiency. These effects have been studied in some depth by us and others in recent years.[14, 15, 18, 48, 61, 62] While bubble formation causes local variations in the thickness of the the ΔpH layer (see discussion of Figs. 2a-c,e above), the flow rate has only a minor influence on the size of the bubbles[63] and will not lead to large variations in bubble morphology.

Limitations and scope of applicability

Despite some limitations in spatial resolution, the data presented above demonstrate that 2D imaging of pH gradients and oxygen concentration profiles using fluorescent foils provides a powerful tool to investigate and understand mass transport limitations in (photo)electrochemical water splitting at device scale. The next steps would be to investigate the influences of electrode spacing, cell height, and tilting angle of the cell, since PEC cells will typically not be oriented vertically (90°) but at an angle that matches the incident angle of sunlight (between 32 – 36° in northern Europe).[64] All these factors will affect the interplay between buoyancy-driven and forced convection, which will in turn affect the pH gradients, bubble dynamics, and transport of dissolved gaseous species.[18] The material and the morphology of the electrodes can also play a role. For example, the use of (nano)structured or porous electrodes will likely lead to different surface wettability and electrolyte flow behaviour. We believe that these factors, however, play a less critical role than buffer concentration and flow rate in affecting pH gradients at device scale. Furthermore, the electrodes in this study were oriented in a parallel 'face-to-face' manner, since it represents the most extensively adopted configuration for fundamental (P)EC investigations.[65] Other PEC designs, however, may be based on back-to-back,[45] louvered,[66, 67] or super-tube arrangements.[68] Also for those designs, the *in situ* mass transport measurements described here can complement and validate numerical simulations [19] and offer key insights into the performance bottlenecks of next-generation PEC devices.

Finally, we note that although a higher buffer concentration effectively suppresses pH gradients, it inevitably introduces additional trade-offs. For instance, pH-neutral buffered electrolytes can induce band-edge pinning,[69] which can be either favorable or unfavorable. Moreover, our previous work revealed that elevated buffer concentrations enlarge bubble size and decrease bubble number density, consequently exacerbating bubble-induced optical losses.[14] Such performance compromises thus require comprehensive evaluation when selecting buffered electrolytes for (photo)electrochemical water splitting applications.

Experimental

Electrochemical measurements

A customized (photo)electrochemical flow cell was designed and constructed in our workshop, see the technical drawing and schematic illustration of the system layout in Fig. S1. Digital photographs of the setup are shown in Fig. S2. The technical drawing of this cell is available from the corresponding authors upon reasonable request. The electrolyte was circulated using a laboratory gear pump (LAB-9, GATHER Industrie). The electrolyte reservoir located at the bottom has an approximate volume of ~400 mL, and a 3D printed plastic structure (VisiJet M2S-HT90) was installed to serve as a flow homogenizer (or flow distributor), as shown by the exploded view of the flow cell in Fig. S1. The electrolyte was mixed in the flow homogenizer before re-entering into channel between two electrodes. Note that the electrolyte flow is driven at a fixed pumping power, such that its volumetric flow rate (mL s^{-1}) remains constant; in contrast, the average flow velocity (mL cm^{-2} s^{-1})—defined as the volumetric flow rate divided by the cross-sectional area—varies with changes in cross-sectional area. For instance, the cross-sectional area of the two-electrode section measures approximately 62 cm^2. Pt-coated FTO electrodes were used as both the anode and cathode. The electrodes were prepared by depositing 100 nm of Pt onto FTO-coated glass substrates (thickness 3 mm, ~10 Ω/sq, Sigma-Aldrich). Before Pt deposition, the FTO substrates were cleaned via sequential ultrasonic rinsing in a soap solution, acetone, isopropanol, 1 M KOH, and Milli-Q water (10 minutes per bath). The Pt deposition was done by electron beam evaporation in a customized high vacuum deposition chamber (Telemark) with a base pressure of 2×10^{-7} mbar. A deposition rate of 0.5 Å s^{-1} was used. To form an electrical connection with the electrodes, a small part of the Pt surface was connected to an electrical wire with a conductive tape (3M), after which the contacts were sealed using epoxy (101RF, purchased from Microset). Potassium phosphate (KP_i) buffer solutions of 0.1M and 1M were prepared from KH_2PO_4 (Sigma-Aldrich, ≥99.0%) and $K_2HPO_4{\cdot}3H_2O$ (Sigma Aldrich, ≥99.0%) to obtain the desired pH (7). An unbuffered 0.5 M potassium sulfate solution (pH 7) was prepared by dissolving K_2SO_4 (Sigma Aldrich, ≥99.0%) in water without adjusting the pH, while a pH 3.5 version of the 0.5 M K_2SO_4 solution was prepared by titrating 0.5 M H_2SO_4 (Fluka Analytical, pH = 0) into the unbuffered solution. The pH of all electrolyte solutions was

View Article Online DOI: 10.1039/D5EE00057F

measured using a calibrated pH meter (FiveEasy pH meter F20-Std-Kit, Mettler Toledo) before each experiment. The water used in all experiments was obtained from a Milli-Q Integral system with a resistivity of 18.2 MΩ cm. The electrolyte solution was purged in a beaker by N_2 bubbling for half an hour before pouring it into the flow cell. All the electrochemical measurements were performed using a two-electrode configuration in galvanostatic mode using a VersaSTAT 3 potentiostat/galvanostat (AMETEK). The current density was kept constant at 10 mA cm^{-2}.

Fluorescence measurements

Fluorescence measurements were conducted by inserting different types of fluorescence foil sensors (pH or O_2 concentration) in between (and perpendicular to) the two electrodes. The fluorescence images were recorded using the VisiSens™ TD Basic System (PreSens), and the schematic illustration and the digital photograph of the setup are shown in Fig. 1a and Fig. S2, respectively. Two different types of pH foil sensors were used for the acidic (initial pH = 3.5, foil sensor: SF-LV1R, PreSens) and neutral (initial pH = 7, foil sensor: SF-HP5R, PreSens) pH electrolyte solutions. The dissolved oxygen concentration was measured using an O_2 sensor foil (SF-RPSu4, PreSens). To eliminate the interference of ambient O_2 dissolution during the oxygen concentration measurements, the headspace of the cell was constantly purged with compressed nitrogen throughout the tests, as illustrated schematically in Fig. S11. As a result, the outflowing gas mixture is primarily N_2, with only trace amounts of evolved O_2 and H_2. The calibration results of the foil sensors can be found in Fig. S3. The pH foil sensor for neutral pH conditions (SF-HP5R) was calibrated with 0.1 M KP_i buffer, and the pH foil sensor for acidic conditions (SF-LV1R) was calibrated with 0.5 M K_2SO_4 solution. The oxygen concentration foil sensor was calibrated in 0.5 M K_2SO_4 solution at 1 bar, and purged with N_2 (Air Liquide, purity ≥ 99.999%, O_2 impurity ≤ 2 ppm), compressed ambient air, or O_2 bubbling (Air Liquide, purity ≥ 99.99%), to achieve 0%, 20.9%, and 100% O_2 concentration in the electrolyte, respectively. The pH foil sensors incorporate green fluorescent pH indicator dyes and inert red fluorescent dye as references. The luminophores were excited by the blue LEDs incorporated with the camera detector. The ratio between the green and the red fluorescent signals, which were collected through the wavelength-separated channels in the RGB camera detector and processed with VisiSens ScientifiCal 1.10 (PreSens), were used for the calibration and the measurements. To guarantee high-quality imaging, the blue LEDs were positioned facing the fluorescent foil sensor, as visualized in the provided photographs and schematic diagrams in Fig. S2. The whole setup was placed in a custom-built 'black box' equipped with laser safety curtains. All laboratory ambient lights were switched off during measurements, and these precautions effectively minimized the influence of the ambient light.

Particle image velocimetry measurements

The flow velocity field between the two parallel electrodes was examined using particle image velocimetry (PIV, LaVision). A schematic illustration and digital photographs of the PIV setup are shown in Fig. S4. Polyamide particles (diameter: 20 μm, density: 1.03 g cm^{-3}) were suspended into the electrolyte (0.1 M KP_i, pH = 7, particle density: ~1 million particles per mL) by overnight stirring. A 532 nm laser (Bernoulli PIV) was used to generate the laser 'sheet' that illuminates the suspended particles. The motion of these particles was captured with a macroscopic camera (Imager MX, LaVision) while the flow velocity of the particles was obtained by software-processing the time-sequenced images (DaVis, LaVision). Since the density of the seeded particles and the electrolyte (0.1 M KP_i, ~1 g cm^{-3}) are nearly identical, the velocity of the electrolyte can be represented by the motions of the particles. An example of the PIV results is shown in Fig. S5.

Conclusions

In summary, we conducted *in situ* measurements on the transport of charged species (e.g., protons and hydroxide ions) and uncharged species (e.g., dissolved oxygen) in aqueous solutions during water splitting under operating conditions that are relevant for practical photoelectrochemical devices. A combination of particle image velocimetry (PIV) and 2D pH measurements using fluorescent foils provided new insights on the influence of electrolyte flow on mass transport processes. Our quantitative findings revealed that the pH gradient can exceed 3 units in unbuffered solutions at 10 mA cm^{-2}, even when mixing and recirculating the electrolyte at a flow rate of 3.2 mL cm^{-2} s^{-1}. This leads to detrimental concentration overpotential losses that can be mitigated by titrating the electrolyte to lower pH, or by using buffered electrolytes with a sufficiently high concentration (e.g., 1 M KP_i buffer solution). At such high buffer concentration, forced electrolyte convection only showed a minor impact on the pH gradient. Moreover, the experimentally observed changes in pH and electrode potential at very low flow rates (<0.05 mL cm^{-2} s^{-1}) are much smaller than those predicted by previously reported 1D multiphysics simulations. This suggests that these simulations cannot yet capture all the physics and should be treated with some caution in the low flow rate regime. An increase in the operating pressure of the device by 4 barg was found to have a negligible effect on the pH gradient. Furthermore, *in situ* observations of dissolved oxygen concentrations during water electrolysis helped identify gas crossover risks in membrane-less devices but also revealed that gas crossover has negligible influence on the reaction thermodynamics (i.e., the Nernst potentials). Collectively, these results demonstrate that integrating straightforward yet powerful characterization tools like fluorescence imaging and PIV provide insights that complement those which can be obtained by numerical modeling and allow identification of critical features such as mass transport limitations and flow dead zones in (P)EC cells under realistic working conditions. The quantitative results from this work help bridge the gap between the fundamental understanding of the mass transport phenomena in (photo)electrochemical reactions and the rational design of scalable energy conversion devices.

Author contributions

Feng Liang: Writing – original draft, Writing – review & editing, Methodology, Investigation, Conceptualization, Data curation. **Fatwa F. Abdi:** Writing – review & editing, Methodology, Conceptualization, Funding acquisition. **Roel van de Krol:** Writing – review & editing, Supervision, Funding acquisition.

Conflicts of interest

The authors declare no competing interests.

Data availability

The datasets presented in the graphs of Figures 2-7 can be obtained from https://doi.org/10.57760/sciencedb.29784. Additional experimental videos and supplementary data are provided in the supplementary information (SI). Supplementary information includes figures (Fig. S1–S10) and video (S1-S7).

Acknowledgements

We gratefully acknowledge the Helmholtz Association of German Research Centers (HGF) and the Federal Ministry of Research, Technology and Space (BMFTR), Germany for supporting the development of solar powered technologies for H_2 generation within the framework of the Innovation Pool project "Solar H_2: Highly Pure and Compressed" and the Helmholtz Research Program "Materials and Technologies for the Energy Transition" (MTET). Part of the work was also carried out with the support of the Helmholtz Energy Materials Foundry (HEMF), a large-scale distributed research infrastructure founded by the German Helmholtz Association (GZ 714-48172-21/1). F.L. also acknowledges support from Xi'an Jiaotong University under the 'Outstanding Young Researcher Program' (JX6J050). F.F.A. acknowledges support from CityUHK (project 9610621) and the Hong Kong Research Grant Council (RGC) under the ANR/RGC Joint Research Scheme (project A-CityU102/24). We also acknowledge Karsten Harbauer for his assistance in the preparation of Pt/FTO electrodes, Christian Höhn, Lars Drescher, and Torsten Wagner for the construction of the customized flow cell, and Dr. Keisuke Obata for his initial effort in establishing the protocols for the fluorescence measurements.

Notes and references

1. N. S. Lewis, *Science* 351 (2016): aad1920.
2. K. Sivula and R. van de Krol, *Nature Reviews Materials* 1 (2016): 1-16.
3. I. Y. Ahmet, Y. Ma, J.-W. Jang, T. Henschel, B. Stannowski, T. Lopes, A. Vilanova, A. Mendes, F. F. Abdi and R. van de Krol, *Sustainable Energy & Fuels* 3 (2019): 2366-2379.
4. H. Nishiyama, T. Yamada, M. Nakabayashi, Y. Maehara, M. Yamaguchi, Y. Kuromiya, Y. Nagatsuma, H. Tokudome, S. Akiyama and T. Watanabe, *Nature* 598 (2021): 304-307.
5. A. Vilanova, T. Lopes and A. Mendes, *Journal of Power Sources* 398 (2018): 224-232.
6. S. Tembhurne, F. Nandjou and S. Haussener, *Nature Energy* 4 (2019): 399-407.
7. I. Holmes-Gentle, S. Tembhurne, C. Suter and S. Haussener, *Nature Energy* 8 (2023): 586-596.
8. J. H. Kim, D. Hansora, P. Sharma, J.-W. Jang and J. S. Lee, *Chemical Society Reviews* 48 (2019): 1908-1971.
9. D. Strmcnik, M. Uchimura, C. Wang, R. Subbaraman, N. Danilovic, D. Van Der Vliet, A. P. Paulikas, V. R. Stamenkovic and N. M. Markovic, *Nature Chemistry* 5 (2013): 300-306.
10. M. Auinger, I. Katsounaros, J. C. Meier, S. O. Klemm, P. U. Biedermann, A. A. Topalov, M. Rohwerder and K. J. Mayrhofer, *Physical Chemistry Chemical Physics* 13 (2011): 16384-16394.
11. K. K. Joshi, P. M. Pataniya, G. Bhadu, P. Sahatiya and C. K. Sumesh, *International Journal of Hydrogen Energy* 96 (2024): 46-58.
12. R. P. Patel, P. M. Pataniya, S. Siraj, P. Sahatiya and C. K. Sumesh, *International Journal of Hydrogen Energy* 55 (2024): 815-827.
13. F. Liang, R. van de Krol and F. F. Abdi, *Nature Communications* 15 (2024): 4944.
14. F. Liang, R. van de Krol and F. F. Abdi, *Chemical Engineering Journal* 512 (2025): 162513.
15. F. Liang, R. van de Krol and F. F. Abdi, *Cell Reports Physical Science* 5 (2024): 102069.
16. M. R. Singh, C. Xiang and N. S. Lewis, *Sustainable Energy & Fuels* 1 (2017): 458-466.
17. M. R. Singh, K. Papadantonakis, C. Xiang and N. S. Lewis, *Energy & Environmental Science* 8 (2015): 2760-2767.
18. K. Obata and F. F. Abdi, *Sustainable Energy & Fuels* 5 (2021): 3791-3801.
19. K. Obata, A. Mokeddem and F. F. Abdi, *Cell Reports Physical Science* 2 (2021): 100358.
20. F. F. Abdi, R. R. G. Perez and S. Haussener, *Sustainable Energy & Fuels* 4 (2020): 2734-2740.
21. A. M. Zimer, M. M. da Silva, E. G. Machado, H. Varela, L. H. Mascaro and E. C. Pereira, *Analytica Chimica Acta* 897 (2015): 17-23.
22. P. Steegstra and E. Ahlberg, *Journal of Electroanalytical Chemistry* 685 (2012): 1-7.
23. M. C. Monteiro and M. T. Koper, *Current Opinion in Electrochemistry* 25 (2021): 100649.
24. F.-M. Boldt, J. Heinze, M. Diez, J. Petersen and M. Börsch, *Analytical Chemistry* 76 (2004): 3473-3481.
25. J. Izquierdo, L. Nagy, Á. Varga, J. J. Santana, G. Nagy and R. M. Souto, *Electrochimica Acta* 56 (2011): 8846-8850.
26. J. O. Park, C. H. Paik and R. Alkire, *Journal of the Electrochemical Society* 143 (1996): L174.
27. B. R. Horrocks, M. V. Mirkin, D. T. Pierce, A. J. Bard, G. Nagy and K. Toth, *Analytical Chemistry* 65 (1993): 1213-1224.
28. D. Bizzotto, *Current Opinion in Electrochemistry* 7 (2018): 161-171.
29. O. Ayemoba and A. Cuesta, *ACS Applied Materials & Interfaces* 9 (2017): 27377-27382.

30. M. Dunwell, X. Yang, B. P. Setzler, J. Anibal, Y. Yan and B. Xu, *ACS Catalysis* 8 (2018): 3999-4008.
31. T. Doneux, L. Bouffier, B. Goudeau and S. Arbault, *Analytical Chemistry* 88 (2016): 6292-6300.
32. N. C. Rudd, S. Cannan, E. Bitziou, I. Ciani, A. L. Whitworth and P. R. Unwin, *Analytical Chemistry* 77 (2005): 6205-6217.
33. W. J. Bowyer, J. Xie and R. C. Engstrom, *Analytical Chemistry* 68 (1996): 2005-2009.
34. L. Bouffier and T. Doneux, *Current Opinion in Electrochemistry* 6 (2017): 31-37.
35. Y. Wang, Z. Cao, Q. Yang, W. Guo and B. Su, *Analytica Chimica Acta* 1074 (2019): 1-15.
36. J. E. Vitt and R. C. Engstrom, *Analytical Chemistry* 69 (1997): 1070-1076.
37. Y. Yokoyama, K. Miyazaki, Y. Miyahara, T. Fukutsuka and T. Abe, *ChemElectroChem* 6 (2019): 4750-4756.
38. F. Zhang and A. C. Co, *Angewandte Chemie International Edition* 59 (2020): 1674-1681.
39. B. P. Nadappuram, K. McKelvey, R. Al Botros, A. W. Colburn and P. R. Unwin, *Analytical Chemistry* 85 (2013): 8070-8074.
40. K. Obata, R. van de Krol, M. Schwarze, R. Schomäcker and F. F. Abdi, *Energy & Environmental Science* 13 (2020): 5104-5116.
41. R. Babu and M. K. Das, *International Journal of Hydrogen Energy* 44 (2019): 14467-14480.
42. M. A. Modestino, K. A. Walczak, A. Berger, C. M. Evans, S. Haussener, C. Koval, J. S. Newman, J. W. Ager and R. A. Segalman, *Energy & Environmental Science* 7 (2014): 297-301.
43. C. A. Rodriguez, M. A. Modestino, D. Psaltis and C. Moser, *Energy & Environmental Science* 7 (2014): 3828-3835.
44. R. A. Marquez, J. T. Bender, S. C. da Cunha, A. M. Aleman, A. Sahu, V. Ganesan, D. J. Milliron, J. Resasco, T. F. Jaramillo and C. B. Mullins, *ACS Energy Letters* 10 (2025): 2075-2083.
45. W.-H. Cheng, M. H. Richter, M. M. May, J. Ohlmann, D. Lackner, F. Dimroth, T. Hannappel, H. A. Atwater and H.-J. Lewerenz, *ACS Energy Letters* 3 (2018): 1795-1800.
46. H. Choi, Y. Y. Kim, S. Seo, Y. Jung, S. M. Yoo, C. S. Moon, N. J. Jeon, S. Lee, K. Lee and F. M. Toma, *Advanced Energy Materials* 13 (2023): 2300951.
47. M. E. Ivanova, R. Peters, M. Müller, S. Haas, M. F. Seidler, G. Mutschke, K. Eckert, P. Röse, S. Calnan and R. Bagacki, *Angewandte Chemie International Edition* 62 (2023): e202218850.
48. F. Liang, H. Kong, D. Suresh Babu, R. van de Krol and F. F. Abdi, *Nature Communications* 16 (2025): 11139.
49. M. A. Modestino, D. F. Rivas, S. M. H. Hashemi, J. G. Gardeniers and D. Psaltis, *Energy & Environmental Science* 9 (2016): 3381-3391.
50. S. Zhang, I. Ahmet, S.-H. Kim, O. Kasian, A. M. Mingers, P. Schnell, M. Kölbach, J. Lim, A. Fischer, K. J. J. Mayrhofer, S. Cherevko, B. Gault, R. van de Krol and C. Scheu, *ACS Applied Energy Materials* 3 (2020): 9523-9527.
51. H. Qiu, K. Obata, Z. Yuan, T. Nishimoto, Y. Lee, K. Nagato, I. Kinefuchi, J. Shiomi and K. Takanabe, *Langmuir* 39 (2023): 4993-5001.
52. I. Holmes-Gentle, F. Bedoya-Lora, F. Alhersh and K. Hellgardt, *The Journal of Physical Chemistry C* 123 (2018): 17-28.
53. D. R. Lide, CRC handbook of chemistry and physics, CRC press (2004).
54. F. Chenlo, R. Moreira, G. Pereira and M. J. Vázquez, *Journal of Chemical & Engineering Data* 41 (1996): 906-909.
55. A. Kuhn and C. Chan, *Journal of Applied Electrochemistry* 13 (1983): 189-207.
56. W. Xing, M. Yin, Q. Lv, Y. Hu, C. Liu and J. Zhang, in Rotating Electrode Methods and Oxygen Reduction Electrocatalysts, eds. W. Xing, G. Yin and J. Zhang, Elsevier, Amsterdam (2014). DOI: https://doi.org/10.1016/B978-0-444-63278-4.00001-X, pp. 1-31.
57. J. Heinrich, F. Ränke, K. Schwarzenberger, X. Yang, R. Baumann, M. Marzec, A. F. Lasagni and K. Eckert, *Langmuir* 40 (2024): 2918-2929.
58. N. I. Kolev, in Multiphase Flow Dynamics 4: Turbulence, Gas Adsorption and Release, Diesel Fuel Properties, ed. N. I. Kolev, Springer Berlin Heidelberg, Berlin, Heidelberg (2012). DOI: 10.1007/978-3-642-20749-5_11, pp. 209-239.
59. W. M. Haynes, D. R. Lide and T. J. Bruno, CRC handbook of chemistry and physics, CRC press (2016).
60. A. Castro-Carranza, P. Vega-Hernández, J. C. Nolasco, A. Ladstätter-Weißenmayer, M. Eickhoff and J. Gutowski, *Physica Status Solidi (a)* 219 (2022): 2100669.
61. P. A. Kempler, R. H. Coridan and N. S. Lewis, *Energy & Environmental Science* 13 (2020): 1808-1817.
62. P. A. Kempler, Z. P. Ifkovits, W. Yu, A. I. Carim and N. S. Lewis, *Energy & Environmental Science* 14 (2021): 414-423.
63. K. Obata, M. Schwarze, T. A. Thiel, X. Zhang, B. Radhakrishnan, I. Y. Ahmet, R. van de Krol, R. Schomäcker and F. F. Abdi, *Nature Communications* 14 (2023): 6017.
64. M. Z. Jacobson and V. Jadhav, *Solar Energy* 169 (2018): 55-66.
65. A. Vilanova, P. Dias, T. Lopes and A. Mendes, *Chemical Society Reviews* 53 (2024): 2388-2434.
66. K. Walczak, Y. Chen, C. Karp, J. W. Beeman, M. Shaner, J. Spurgeon, I. D. Sharp, X. Amashukeli, W. West and J. Jin, *ChemSusChem* 8 (2015): 544-551.
67. B. Turan, J.-P. Becker, F. Urbain, F. Finger, U. Rau and S. Haas, *Nature Communications* 7 (2016): 12681.
68. M. M. May, D. Lackner, J. Ohlmann, F. Dimroth, R. van de Krol, T. Hannappel and K. Schwarzburg, *Sustainable Energy & Fuels* 1 (2017): 492-503.
69. Y. Kageshima, H. Kumagai, K. Teshima, K. Domen and H. Nishikiori, *Chemical Science* 16 (2025): 14088-14097.

View Article Online
DOI: 10.1039/D6EL00057F

The datasets presented in the graphs of Figures 2-7 can be obtained from https://doi.org/10.57760/sciencedb.29784. Additional experimental videos and supplementary data are provided in the supplementary information (SI). Supplementary information includes figures (Fig. S1-S10) and video (S1-S7).